Fast calculation of carrier harmonic iron losses caused by pulse width modulation in interior permanent magnet synchronous motors

Zhu, Sa; Dong, Jianning; Li, Yanru; Hua, Wei

DOI
10.1049/iet-epa.2019.0837

Publication date
2020

Document Version
Final published version

Published in
IET Electric Power Applications

IET Electric Power Applications

Research Article

IET Journals
The Institution of Engineering and Technology

Fast calculation of carrier harmonic iron losses caused by pulse width modulation in interior permanent magnet synchronous motors

ISSN 1751-8660
Received on 5th October 2019
Revised 2nd February 2020
Accepted on 27th February 2020
E-First on 12th May 2020
doi: 10.1049/iet-epa.2019.0837
www.ietdl.org

Sa Zhu[1] ✉, *Jianning Dong*[2], *Yanru Li*[1], *Wei Hua*[3]

[1]*Department of Energy and Electrical Engineering, Hohai University, Nanjing, People's Republic of China*
[2]*Department of Electrical Sustainable Energy, Delft University of Technology, Delft 2628CD, The Netherlands*
[3]*Department of Electrical Engineering, Southeast University, Nanjing, People's Republic of China*
✉ *E-mail: zhusa@hhu.edu.cn*

Abstract: Normal calculation of the carrier harmonic iron losses (CHILs) brought by the pulse width modulated (PWM) voltage source inverter in interior permanent magnet synchronous motors by the time-stepping finite-element analysis (TSFEA) with short time steps is very time-consuming. In this study, a novel method for fast calculation is proposed, where a combination of the frozen differential reluctivity tensor method and the time-harmonic finite-element analysis is proposed to investigate the relationship between PWM voltage harmonics and the corresponding CHILs, with which the CHILs in stator and rotor are fast-calculated with the voltage harmonics in stator and rotor reference frames, respectively. Besides, the eddy current reaction effect in electrical steel sheets on the CHILs at high frequency is considered by an analytical method and validated with the TSFEA. The results reveal that eight parameters are recommended to calculate the CHILs at different operating conditions, which vary with the fundamental current. Consequently, the CHIL map over the entire operating conditions can be fast-calculated using the analytical spectra of the PWM voltages. Experiment on a specimen is conducted to validate the accuracy of the proposed method, which shows it depends on whether the equivalent differential permeability of the silicon steel can be accurately modelled.

1 Introduction

Interior permanent magnet synchronous motors (IPMSMs) are widely applied in electric vehicles (EVs) and hybrid EVs, due to their high efficiency, high power/torque density, and wide speed range [1, 2]. Improving the efficiency of IPMSMs is the target for motor designers [3] and drive developers [4], which needs accurate iron loss modelling.

Traditional finite-element analysis (FEA) [5, 6] using the sinusoidal current source (SCS) excitation is unable to calculate the carrier harmonic iron losses (CHILs) in electrical steel sheets (ESSs) and the harmonic losses in permanent magnets (PMs) brought by the pulse width modulated (PWM) voltage source inverter (VSI), which have been shown to significantly affect the total loss when the IPMSM works at low-torque and low-speed region [7].

The coupled field-circuit time-stepping finite-element analysis (TSFEA) using the PWM voltage as input can be used to calculate the harmonic losses [8], which however needs short time steps to distinguish the harmonics. Hence, it is very time-consuming and resource-consuming for iron-loss mapping over an entire working range and for the optimal design to compare different candidates [3].

In addition, the effect of eddy current induced reaction field has to be considered for accurately calculating the CHILs [9, 10], increasing the difficulty of the problem. The analytical model in [9] is fast and elegant but it is based on the assumption that the permeability of the ESSs is linear, which is not the case for the IPMSM with heavy local oversaturation. One-dimensional (1D) non-linear TSFEA can be used to solve the flux density distribution in one ESS along the thickness direction, by which the reaction field and the non-linearity of the ESSs can be considered [10]. However, the post-processing of 1D TSFEA in each element of the ESSs further increases the calculation time. Besides, experiment results shown in [3] revealed that the 1D non-linear TSFEA method in [10] may underestimate the iron loss under PWM VSI supply. Hence, its accuracy needs further investigation.

A method was proposed in [11, 12] for fast calculating the iron losses of the PWM-fed induction machines directly with the PWM voltage. Although the reaction field was not considered, it is instructive because it shows that there are direct correlations between the CHILs and the PWM voltage harmonics.

Recently, a method for fast calculating the PM eddy current losses caused by PWM voltage harmonics in the IPMSM over the entire working range was proposed in [13], which is based on the combination of the frozen differential reluctivity tensor method (FDRTM) [14, 15] and the linear time-harmonic finite-element analysis (THFEA) [16]. The key idea of this method is that the flux density variations generated by the harmonic voltages are too small to affect the saturation of the ESSs. Hence, the FDRTM can be applied to obtain the locally linearised model of the IPMSM, which is also named as the small-signal model of the IPMSM [14]. Based on this model, the relationship between harmonic voltages and the corresponding flux density variations can be conveniently studied.

In this paper, the combination of the FDRTM and the linear THFEA is further proposed to investigate the relationships between PWM voltage harmonics and the corresponding CHILs in the ESSs. The conductivity of the PMs is simply set to be zero in this paper to focus on the CHILs. With the small-signal model of the IPMSM, the analytical iron loss model considering the eddy current reaction field [9] can be applied without worrying about the non-linearity of the ESSs. With the functional relationship between the PWM voltage harmonics and the corresponding CHILs, the total CHILs in the rotor and the stator are proposed to be calculated with the analytical spectra of the PWM voltages in the rotor and the stator reference frames, respectively. Eight parameters are proposed to calculate the CHILs at different operating conditions, which result in functions of the fundamental current and are fitted with the quadratic polynomials. Finally, with the fitted polynomials and the analytical spectra of the PWM voltages [17], the CHIL map over the entire operating range can be obtained.

Table 1 Parameters of the IPMSM in Prius 2010

phases and poles	3 phases, 8 poles
DC voltage of inverter, U_{dc}	650 V
carrier frequency, f_c	4.8 kHz
phase resistance, R_s	0.09 Ω
PM remanence, B_r	1.22T (@114°C)
maximum amplitude of current, I_m	200 A
stator outer diameter	264 mm
axial lamination length	49.3 mm

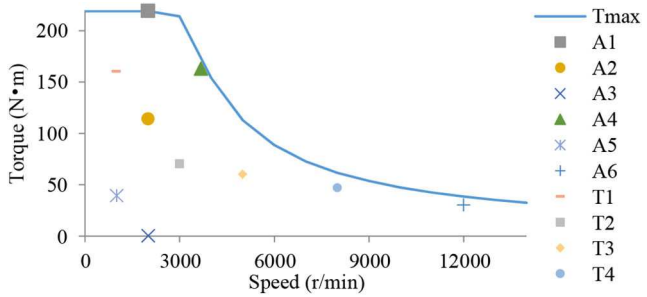

Fig. 1 *Distribution of ten operating conditions*

Table 2 Peak values of the *d*- and *q*-axis currents at ten working conditions

	A1	A2	A3	A4	A5
i_{d0}, A	−149.8	−64.9	0	−149.8	−18.62
i_{q0}, A	132.5	76.04	0	76.04	35.4
speed, r/min	2000	2000	2000	3665	1000
torque, N•m	219.3	113.9	0	162.8	39.3
	A6	T1	T2	T3	T4
i_{d0}, A	−75.25	−98.6	−36.24	−53.25	−75.25
i_{q0}, A	15.9	99.45	53.47	37.75	25.0
speed, r/min	12,000	1000	3000	5000	8000
torque, N•m	30.0	159.9	70.0	59.9	46.8

Table 3 Iron loss coefficients [11]

k_e, W/m^3/Hz^2/T^2	k_h, W/m^3/Hz/T^2	Thickness, mm	Density, kg/m^3
0.585	140	0.35	7650

This paper is structured as follows: in Section 2, the iron losses at one operating point are calculated to show the detailed procedure of the proposed method. The CHILs calculated with the proposed method are verified by the TSFEA [8, 10]. In Section 3, the CHIL maps at different operating conditions are shown. In Section 4, an experiment on a specimen is conducted to verify the effectiveness of the proposed method. Experiment results show the difficultly in accurately modelling the differential permeability of the ESSs due to the hysteresis effect, which is also the reason why the method in [10] may underestimate the CHILs. In Section 5, conclusions are drawn.

2 Fast calculation at one operating point

The IPMSM in Prius 2010 is used as the target motor for calculation, and its parameters are summarised in Table 1 [1, 13, 18]. Fig. 1 shows the distribution of ten operating conditions on the torque-speed map. The fundamental *d*-axis current i_{d0}, the *q*-axis current i_{q0}, and speed at these operating conditions are shown in Table 2. The relationship between the PWM voltage harmonics and the resulting CHILs will be investigated at different operating conditions, respectively. In this section, the operating condition A2, which is the same as working condition B in [13], is chosen as an example for the calculation.

2.1 Iron loss calculation with the TSFEA neglecting eddy current reaction effect

The iron loss P_{iron} is first calculated with the flux density waveform in each element of the ESSs obtained from the TSFEA with [8]:

$$P_{\text{iron}} = \int_{\text{Iron}} \sum_n k_e \cdot (nf)^2 \cdot \left(B_{r,n}^2 + B_{\theta,n}^2\right) \mathrm{d}v + \int_{\text{Iron}} \sum_n k_h \cdot (nf) \cdot \left(B_{r,n}^2 + B_{\theta,n}^2\right) \mathrm{d}v \quad (1)$$

where k_e is the eddy current loss coefficient and k_h is the hysteresis loss coefficient. f is the fundamental frequency of the alternating flux density. $B_{r,n}$ and $B_{\theta,n}$ are the nth harmonics of the radial and peripheral components of the flux density, respectively. The excess loss is neglected or considered to have been incorporated into k_e for simplification [8–10]. Besides, the rotational losses are simply calculated by independently summing the losses generated by the radial and tangential components of the flux density variation. Although the accuracy may be sacrificed, it is a very common practice to use the simple iron loss models having only classical eddy current and hysteresis terms for calculating iron losses in electrical machines [3, 7–12, 19–22] for engineering applications.

The thickness of the ESSs used in the target motor is 0.35 mm, but the iron loss coefficients are unavailable in [1]. Hence, the loss coefficients of '2735' obtained from the test data below 150 Hz shown in [11] are used for the calculation, as shown in Table 3. Although k_e and k_h may change with the flux density [19, 20], they are assumed to be constant for comparing with the method in [10] where k_e had to be constant.

With the method in [8], naturally sampled space vector PWM strategy is used to generate the PWM voltage based on the parameters of the inverter shown in Table 1 and the on-load back EMF obtained from the TSFEA using the SCS excitation [13]. Then, the coupled field-circuit 2D TSFEA under PWM VSI supply is used to compute the flux density waveform of each element. The time step is set to 1/4800/112 s to distinguish the dominant PWM voltage harmonics around $2f_c$, which means there are 4032 steps in one electrical period at operating point A2, where the fundamental frequency f_o is 400/3 Hz because the speed is 2000 r/min and the pole number is 8 [13]. By applying the fast Fourier transform on the flux density waveform in one electrical period, the amplitude and frequency of each harmonic component are obtained. Then, the iron loss can be calculated with (1).

For comparison, the iron losses using the sinusoidal voltage source (SVS) and SCS excitations are also calculated. When simulating the model with SCS and SVS excitations, the time step is set to 1/4800/4 s and there are 144 steps in one electrical period. The eddy current reaction effects in the ESSs and the PMs are neglected during the FEA. In addition, the iron losses calculated with SCS and SVS supplies having 4032 steps in one period are shown for a fair comparison with the losses calculated with PWM VSI supply. When generating the PWM voltage numerically, the given modulation ratio and phase angle have been carefully turned to make the fundamental component in the generated PWM waveform as close as possible to the sinusoidal voltage applied for calculating the iron loss under SVS supply. The iron losses calculated with different excitations and different numbers of steps are summarised in Table 4. It is found that although fined meshes are used in the airgap region to improve the accuracy, large numerical errors still exist due to the short-term analysis in the calculated iron losses under SCS excitation when there are 4032 steps in one period. However, fortunately, the numerical errors due to the short-term analysis are limited using SVS and PWM VSI excitations.

Fig. 2 shows the eddy current losses in the stator and the rotor calculated with different source supplies, respectively. It can be

Table 4 Comparison of iron losses calculated with different methods when neglecting the eddy current reaction effect

Method		Time, min	Eddy current loss, W		Hysteresis loss, W	
			Stator	Rotor	Stator	Rotor
TS_SCS_144		3.5	60.7	12.1	79.1	1.7
TS_SCS_4032		117.4	~~84.2~~	12.3	79.1	1.7
TS_SVS_144		3.5	59.9	11.7	78.7	1.6
TS_SVS_4032		103.8	60.4	11.9	78.7	1.6
TS_PWM_4032		105.5	139.5	27.5	80.1	1.9
TSFEA	CHIL	—	**79.1**	**15.6**	**1.4**	**0.3**
Proposed	CHIL	4.0	**77.7**	**15.8**	**1.6**	**0.3**

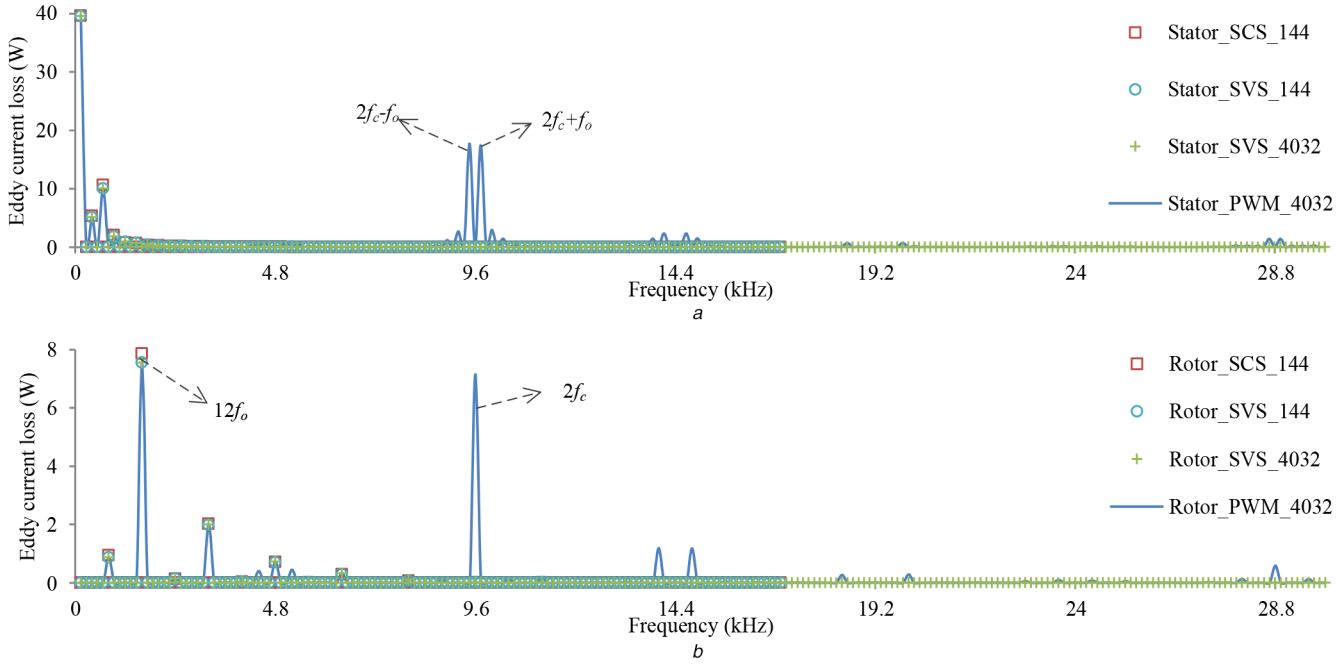

Fig. 2 *Spectra of eddy current loss in the ESSs at operating condition A2 where f_o is 400/3 Hz and f_c is 4800 Hz*
(a) Stator, ***(b)*** Rotor

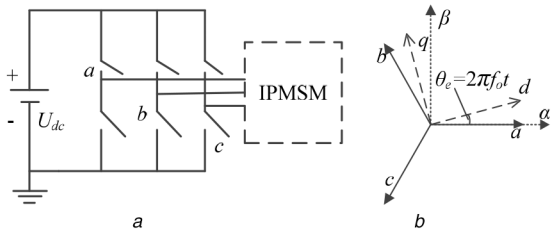

Fig. 3 *Diagram of the inverter-motor system*
(a) PWM VSI, ***(b)*** Different reference frames

seen that the losses generated by the harmonic voltages make up a large proportion in the total losses [8]. Theoretically, the CHIL at up to 268.8 kHz can be obtained because the sample time is 1/4800/112 s. In the following calculation, all the CHILs at different frequencies are computed and summed to obtain the total CHIL. However, only the CHILs below 30 kHz are shown to illustrate the preponderant components clearly, because the CHILs at high frequency are very small.

Also, note that the most preponderant CHILs are at $2f_c \pm f_o$ in the stator, while the most preponderant component in the rotor is at $2f_c$, which is related to the PWM voltages' spectra in different reference frames and will be discussed in the following subsections.

2.2 PWM voltage harmonics in different reference frames

Fig. 3*a* shows the diagram of the PWM VSI and Fig. 4 shows the spectra of the line-line voltage at operating condition A2. It can be seen that each dominant PWM voltage harmonic is symmetrical in the three-phase system and has either a positive or negative sequence [13, 18]. Because of the rotation of the rotor, the $2f_c - f_o$ component having a negative sequence and the $2f_c + f_o$ component having a positive sequence will both induce $2f_c$ flux density variations in the rotor. Hence, it was proposed that the carrier harmonic losses in the PM should be calculated with the PWM voltage harmonics in the rotor reference frame [13]. For the same reason, the CHILs in the rotor should also be calculated with the voltage harmonics in the rotor reference frame. However, the CHILs in the stator should be calculated in the stator reference frame.

The stator reference frame is denoted as $\alpha\beta$ and the rotor reference frame is denoted as dq, as shown in Fig. 3*b*. The PWM voltage in dq reference frame, u_d^{pwm} and u_q^{pwm}, can be calculated by the following equation:

$$\begin{bmatrix} u_d^{\text{pwm}} \\ u_q^{\text{pwm}} \end{bmatrix} = \frac{2}{3} \begin{bmatrix} \cos(\theta_e) & \cos\left(\theta_e - \frac{2\pi}{3}\right) & \cos\left(\theta_e + \frac{2\pi}{3}\right) \\ -\sin(\theta_e) & -\sin\left(\theta_e - \frac{2\pi}{3}\right) & -\sin\left(\theta_e + \frac{2\pi}{3}\right) \end{bmatrix} \begin{bmatrix} v_{ao} \\ v_{bo} \\ v_{co} \end{bmatrix} \quad (2)$$

where v_{ao}, v_{bo} and v_{co} are three-phase voltages. θ_e is the rotor electrical angle. When θ_e is set to 0, (2) can be used to calculate the PWM voltage in the $\alpha\beta$ reference frame, which is denoted as u_α^{pwm} and u_β^{pwm}.

Figs. 5 and 6 show the spectra of the PWM voltages in the dq and $\alpha\beta$ reference frames, respectively. The amplitude of each preponderant component in u_α^{pwm} is equal to that in u_β^{pwm} and the phase difference between them is either 270° or 90°, which shows

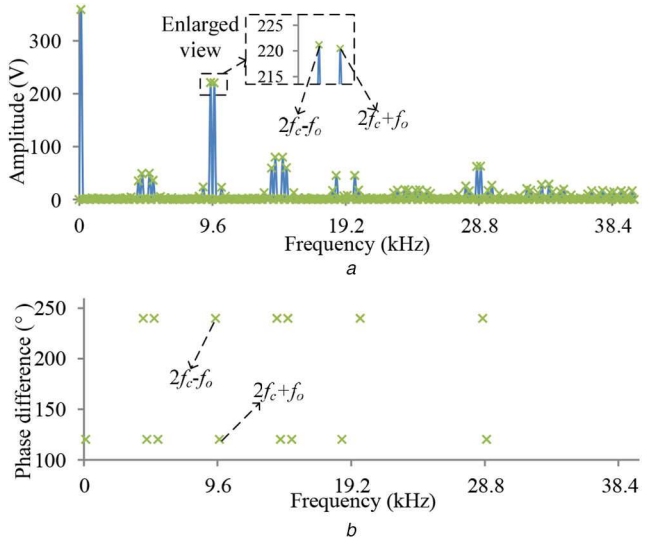

Fig. 4 *Spectra of line-line voltage at working condition A2 where f_o is 400/3 Hz, f_c is 4800 Hz, and the modulation ratio is 0.6345*

(a) Amplitude of each component in u_{ab} below 40 kHz, ***(b)*** Phase differences between preponderant components in u_{ab} and u_{bc}

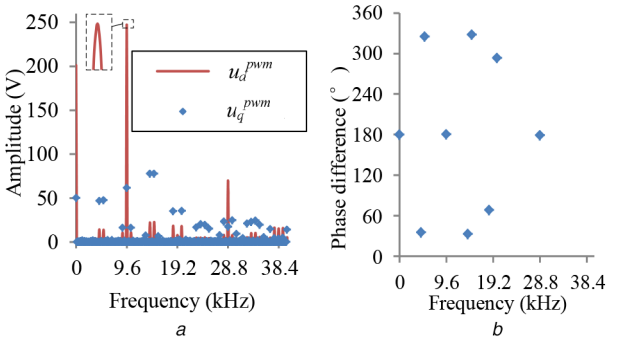

Fig. 5 *PWM voltage spectra in the dq reference frame*

(a) Amplitudes, ***(b)*** Phase difference between each preponderant component in u_d^{pwm} and u_q^{pwm}

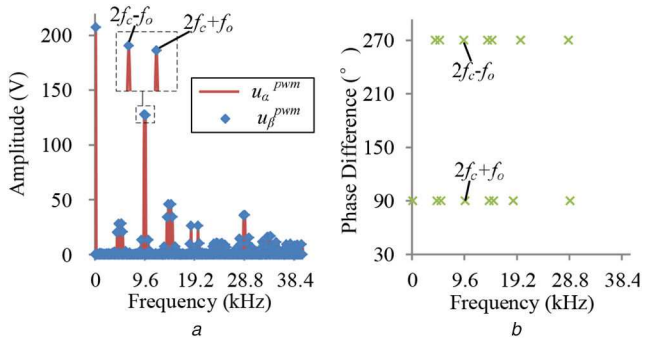

Fig. 6 *PWM voltage spectra in the αβ reference frame*

(a) Amplitudes, ***(b)*** Phase difference between each preponderant component in u_α^{pwm} and u_β^{pwm}

that each PWM voltage harmonic forms a rotating voltage vector in the $\alpha\beta$ reference frame. However, the distribution of the PWM voltage harmonics in the dq reference frame has no general rule [13]. The most dominant harmonic in u_d^{pwm} is at 9.6 kHz, which is in accordance with the spectra of the rotor eddy current loss shown in Fig. 2*b*. Besides, as shown in Fig. 6, the frequencies of the preponderant components in $\alpha\beta$ reference frame are in accordance with the preponderant CHILs in the stator shown in Fig. 2*a*. This reveals there exist correlations between the CHILs in the stator and the rotor with the harmonic voltages in the $\alpha\beta$ and dq reference frames, respectively.

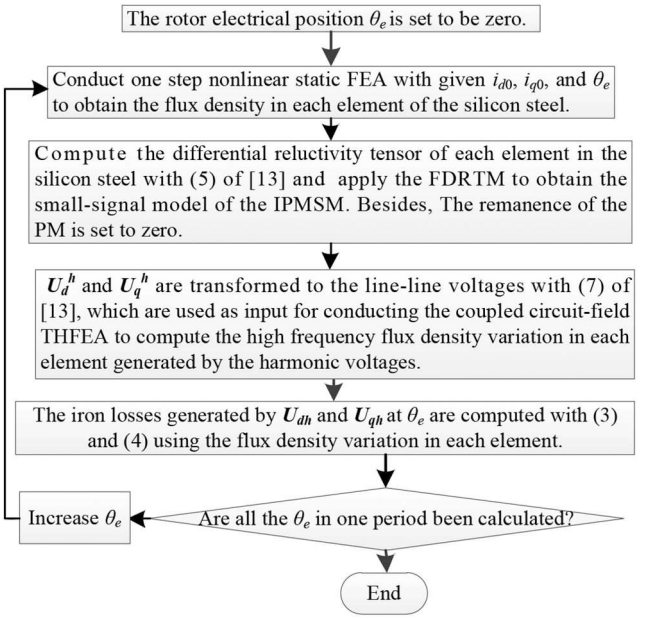

Fig. 7 *Procedure to compute the iron losses caused by one harmonic voltage at a given working condition*

2.3 Fast calculation of CHILs when neglecting the eddy current reaction effect

The procedure to calculate the CHIL caused by one specific PWM voltage harmonic, the d-axis harmonic voltage $\boldsymbol{U}_d^{\text{h}}$ or the q-axis harmonic voltage $\boldsymbol{U}_q^{\text{h}}$, is shown in Fig. 7. With the flux density variation in each element of the ESSs, the eddy current and hysteresis losses can be calculated with:

$$P_{\text{eddy}}^{\text{h}} = \int_{\text{Iron}} k_{\text{e}} \cdot f_{\text{h}}^2 \cdot \left(B_{\text{r,r}}^2 + B_{\text{r,i}}^2 + B_{\theta,\text{r}}^2 + B_{\theta,\text{i}}^2\right) \cdot \text{d}v \tag{3}$$

$$P_{hys}^{h} = \int_{\text{Iron}} k_h \cdot f_h \cdot \left(B_{r,r}^2 + B_{r,i}^2 + B_{\theta,r}^2 + B_{\theta,i}^2\right) \cdot \text{d}v \tag{4}$$

where $B_{\text{r,r}}$ and $B_{\text{r,i}}$ are the real and imaginary parts of the radial flux density component, respectively. $B_{\theta,\text{r}}$ and $B_{\theta,\text{i}}$ are the real and imaginary parts of the peripheral flux density component, respectively. f_{h} is the frequency of the harmonic voltage.

Fig. 8 shows the variations of the stator and rotor eddy current losses with θ_{e} under $\boldsymbol{U}_d^{\text{h}}$ or $\boldsymbol{U}_q^{\text{h}}$ excitation when their frequency f_{h} is set to be 10 kHz. θ_{e} has a significant influence on the iron losses in both the stator and rotor under the same harmonic voltage excitation, which is similar to the PM eddy current loss shown in [13]. Besides, the variation has a period of 60 electrical degrees. To overcome this problem, the eddy current losses obtained at different rotor electrical angles, which distribute uniformly over one period, are averaged to obtain the average value. Table 5 shows the obtained average values when there are different sampling numbers in one period of 60 electrical degrees. It can be seen that the results obtained with 15 sampling points in one period have been very close to those obtained with 60 sampling points in one period. However, increasing the sampling number means increasing the calculation time. Hence, from now on, all the calculated iron eddy current and hysteresis losses will be the average value over one period with 15 sampling points by default.

Because the flux density variation is proportional to the voltage and inversely proportional to the frequency [12], simple equations are assumed for calculating the iron loss under $\boldsymbol{U}_d^{\text{h}}$ or $\boldsymbol{U}_q^{\text{h}}$ excitation independently when neglecting the eddy current reaction effect in the ESSs, which are shown as:

$$P_{d\text{h}}^{\text{s}} = \chi_d^{\text{s}} U_{d\text{h}}^2 (1 + k_{\text{h}}/k_{\text{e}}/f_{\text{h}}), \quad P_{d\text{h}}^{\text{r}} = \chi_d^{\text{r}} U_{d\text{h}}^2 (1 + k_{\text{h}}/k_{\text{e}}/f_{\text{h}}) \tag{5}$$

$$P_{q\mathrm{h}}^{\mathrm{s}} = \chi_q^{\mathrm{s}} U_{q\mathrm{h}}^2 (1 + k_{\mathrm{h}}/k_{\mathrm{e}}/f_{\mathrm{h}}), \quad P_{q\mathrm{h}}^{\mathrm{r}} = \chi_q^{\mathrm{r}} U_{q\mathrm{h}}^2 (1 + k_{\mathrm{h}}/k_{\mathrm{e}}/f_{\mathrm{h}}) \tag{6}$$

where $P_{d\mathrm{h}}{}^{\mathrm{s}}$ and $P_{q\mathrm{h}}{}^{\mathrm{s}}$ are the stator iron losses caused by $\boldsymbol{U_d}^{\mathrm{h}}$ and $\boldsymbol{U_q}^{\mathrm{h}}$, respectively, while $P_{d\mathrm{h}}{}^{\mathrm{r}}$ and $P_{q\mathrm{h}}{}^{\mathrm{r}}$ are the rotor iron losses in the rotor caused by $U_d{}^{\mathrm{h}}$ and $U_q{}^{\mathrm{h}}$, respectively. $U_{d\mathrm{h}}$ and $U_{q\mathrm{h}}$ are amplitudes of $\boldsymbol{U_d}^{\mathrm{h}}$ and $\boldsymbol{U_q}^{\mathrm{h}}$, respectively. $\chi_d{}^{\mathrm{s}}$, $\chi_d{}^{\mathrm{r}}$, $\chi_q{}^{\mathrm{s}}$, and $\chi_q{}^{\mathrm{r}}$ are constant eddy current loss factors.

Table 6 shows the calculated losses from THFEA under $\boldsymbol{U_d}^{\mathrm{h}}$ or $\boldsymbol{U_q}^{\mathrm{h}}$ excitation independently. It is easy to see that eddy current loss is proportional to the square of the voltage and has nothing to do with f_{h} by comparing cases 1, 3, 4, 5, and 6. Hysteresis loss is also proportional to the square of voltage but is inversely proportional to the frequency. Besides, the phase angle does not influence the losses by comparing cases 1 and 2. The results exactly verify the models shown in (5) and (6).

Hence $\chi_d{}^{\mathrm{s}}$, $\chi_d{}^{\mathrm{r}}$, $\chi_q{}^{\mathrm{s}}$, and $\chi_q{}^{\mathrm{r}}$ can be identified with the results shown in cases 1 and 5, which are shown in Table 7. Then, the losses caused by all the other harmonic voltages in Table 6 can be directly calculated with (5) and (6) without repeating the THFEA.

However, $\boldsymbol{U_d}^{\mathrm{h}}$ and $\boldsymbol{U_q}^{\mathrm{h}}$ are always injected to the IPMSM together. For simplicity, it is assumed that the losses generated by the combination of $\boldsymbol{U_d}^{\mathrm{h}}$ and $\boldsymbol{U_q}^{\mathrm{h}}$ can be calculated separately. For the stator, the PWM voltage harmonics in $\alpha\beta$ reference frame are used as input to calculate the losses according to the analysis in previous subsections. Then, the losses in stator and rotor caused by mth order harmonic voltage can be expressed as:

$$\begin{aligned} P_m^{\mathrm{s}\_n} &= P_{m,\mathrm{e}}^{\mathrm{s},\alpha} + P_{m,\mathrm{h}}^{\mathrm{s},\alpha} + P_{m,\mathrm{e}}^{\mathrm{s},\beta} + P_{m,\mathrm{h}}^{\mathrm{s},\beta} \\ &= \chi_d^{\mathrm{s}} U_{\alpha m}^2 + \chi_d^{\mathrm{s}} U_{\alpha m}^2 \cdot \frac{k_{\mathrm{h}}}{k_{\mathrm{e}} f_m^{\alpha\beta}} + \chi_q^{\mathrm{s}} U_{\beta m}^2 + \chi_q^{\mathrm{s}} U_{\beta m}^2 \cdot \frac{k_{\mathrm{h}}}{k_{\mathrm{e}} f_m^{\alpha\beta}} \end{aligned} \tag{7}$$

$$\begin{aligned} P_m^{\mathrm{r}\_n} &= P_{m,\mathrm{e}}^{\mathrm{r},d} + P_{m,\mathrm{h}}^{\mathrm{r},d} + P_{m,\mathrm{e}}^{\mathrm{r},q} + P_{m,\mathrm{h}}^{\mathrm{r},q} \\ &= \chi_d^{\mathrm{r}} U_{dm}^2 + \chi_d^{\mathrm{r}} U_{dm}^2 \cdot \frac{k_{\mathrm{h}}}{k_{\mathrm{e}} f_m^{dq}} + \chi_q^{\mathrm{r}} U_{qm}^2 + \chi_q^{\mathrm{r}} U_{qm}^2 \cdot \frac{k_{\mathrm{h}}}{k_{\mathrm{e}} f_m^{dq}} \end{aligned} \tag{8}$$

where $U_\alpha{}^m$ and $U_\beta{}^m$ are amplitudes of the mth order harmonic voltages in the $\alpha\beta$ reference frame, respectively, while $U_d{}^m$ and $U_q{}^m$ are amplitudes of the mth order harmonic voltages in the dq reference frame, respectively. $P_{m,\mathrm{e}}^{\mathrm{s},\alpha}$, $P_{m,\mathrm{e}}^{\mathrm{s},\beta}$, $P_{m,\mathrm{h}}^{\mathrm{s},\alpha}$, and $P_{m,\mathrm{h}}^{\mathrm{s},\beta}$ $^{\beta}$ are the eddy current and hysteresis losses generated by $U_\alpha{}^m$ and $U_\beta{}^m$ in the stator, respectively. $P_{m,\mathrm{e}}^{\mathrm{r},d}$, $P_{m,\mathrm{e}}^{\mathrm{r},q}$, $P_{m,\mathrm{h}}^{\mathrm{r},d}$ and $P_{m,\mathrm{h}}^{\mathrm{r},q}$ are the eddy current and hysteresis losses generated by $U_d{}^m$ and $U_q{}^m$ in the rotor,

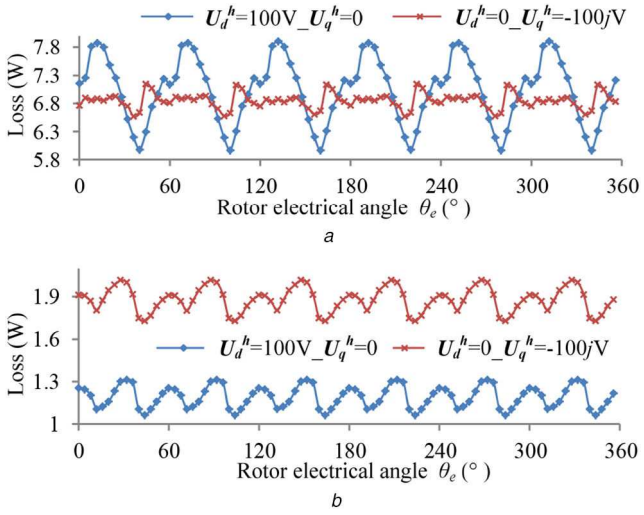

Fig. 8 *Variations of eddy current losses with θ_e at operating condition A2 under different harmonic voltage excitations*
(a) Stator, ***(b)*** Rotor

Table 5 Average values of the eddy current losses obtained with different sampling numbers in one period

Sampling number in one period	$\boldsymbol{U_d^h}$ = 100V_$\boldsymbol{U_q^h}$ = 0		$\boldsymbol{U_d^h}$ = 0V_$\boldsymbol{U_q^h}$ = 100V	
	Rotor	Stator	Rotor	Stator
2	1.282	6.936	1.959	6.785
5	1.198	7.043	1.876	6.840
10	1.194	7.012	1.878	6.842
15	1.191	7.030	1.879	6.849
30	1.192	7.024	1.879	6.854
60	1.192	7.022	1.879	6.852

Table 6 Iron losses under $\boldsymbol{U_d}^{\mathrm{h}}$ or $\boldsymbol{U_q}^{\mathrm{h}}$ excitation

Case	$\boldsymbol{U_d}^{\mathrm{h}}$, V	$\boldsymbol{U_q}^{\mathrm{h}}$, V	f_{h} ,kHz	Eddy current loss, W		Hysteresis loss, W	
				Stator	Rotor	Stator	Rotor
1	100	0	10	7.03	1.19	0.17	0.03
2	$100e^{j90°}$	0	10	7.03	1.19	0.17	0.03
3	200	0	10	28.12	4.76	0.67	0.11
4	100	0	5	7.03	1.19	0.34	0.06
5	0	100	10	6.85	1.88	0.16	0.04
6	0	200	10	27.4	7.51	0.66	0.18

Table 7 Parameters for calculating the CHILs at different operating conditions

	A3	A5	A2	A6	A4	A1
χ_d^s, 10^{-4}W/V^2	6.38	6.47	7.03	6.26	6.46	7.27
χ_d^r, 10^{-4}W/V^2	1.06	1.44	1.19	0.68	0.81	0.98
χ_q^s, 10^{-4}W/V^2	5.08	5.70	6.85	5.45	7.07	8.09
χ_q^r, 10^{-4}W/V^2	2.38	2.35	1.88	1.99	2.60	1.76
μ_{dh}^s/μ_0	5076	3849	2760	6967	3695	1989
μ_{dh}^r/μ_0	2849	1862	1474	3498	1570	1286
μ_{qh}^s/μ_0	6609	2711	1387	5999	2198	951
μ_{qh}^r/μ_0	5211	1452	957	5168	1576	806

Table 8 Iron losses under different combinations of $\boldsymbol{U_d}^h$ and $\boldsymbol{U_q}^h$ excitation when f_h is 10 kHz

Case	$\boldsymbol{U_d}^h$, V	$\boldsymbol{U_q}^h$, V	THFEA, W		Independently sum, W		Relative error	
			Stator	Rotor	Stator	Rotor	Stator, %	Rotor, %
7	$100e^{j0°}$	$100e^{-j90°}$	14.21	3.14	14.21	3.14	0.00	0.00
8	$100e^{j0°}$	$100e^{j0°}$	15.09	3.47	14.21	3.14	−5.83	−9.51
9	$100e^{j0°}$	$100e^{j45°}$	14.84	3.38	14.21	3.14	−4.25	−7.10
10	$100e^{j0°}$	$100e^{j90°}$	14.21	3.14	14.21	3.14	0.00	0.00
11	$100e^{j0°}$	$100e^{j135°}$	13.59	2.91	14.21	3.14	4.56	7.90
12	$100e^{j0°}$	$100e^{j180°}$	13.32	2.82	14.21	3.14	6.68	11.35
13	$247.3e^{j7.4°}$	$62.2e^{j186.3°}$	45.36	7.70	46.72	8.20	3.00	6.55
14	$22.8e^{j174.3°}$	$78.1e^{j140.9°}$	4.79	1.29	4.66	1.24	−2.75	−3.79

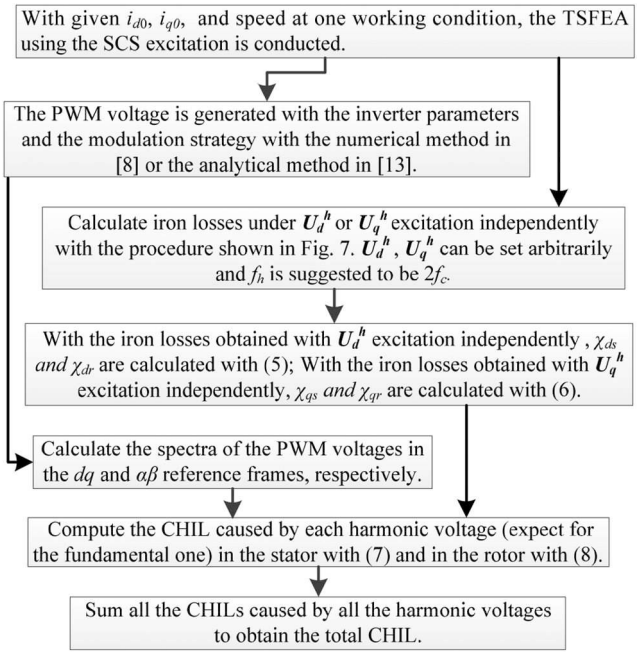

Fig. 9 *Calculation of the total CHIL at a given working condition when neglecting the eddy current reaction effect*

respectively. $f_m^{\alpha\beta}$ and f_m^{dq} are the frequencies of the mth order harmonics in $\alpha\beta$ and dq reference frames, respectively.

When f_h is 10 kHz, the losses obtained with the THFEA under different harmonic combination excitations are compared with those calculated by the sum of the iron losses caused by $\boldsymbol{U_d}^h$ and $\boldsymbol{U_q}^h$ independently, as shown in Table 8. According to cases 7 and 10, it can be concluded that when the phase difference between $\boldsymbol{U_d}^h$ and $\boldsymbol{U_q}^h$ is 90° and their amplitudes are equal, the iron loss caused by the combination of $\boldsymbol{U_d}^h$ and $\boldsymbol{U_q}^h$ is equal to the sum of the iron losses caused by $\boldsymbol{U_d}^h$ and $\boldsymbol{U_q}^h$ independently. For the stator, the PWM voltage harmonics in $\alpha\beta$ reference frame just satisfy this condition. Hence, the losses in stator can be exactly calculated with (7).

For the rotor, there is no general rule for the phase difference between $\boldsymbol{U_d}^h$ and $\boldsymbol{U_q}^h$ according to Fig. 5. Besides, their amplitudes are also not equal. Comparing the cases from 7 to 14, when the phase differences are not equal to 90° or −90°, the iron losses caused by the combination of $\boldsymbol{U_d}^h$ and $\boldsymbol{U_q}^h$ are not equal to those calculated by independently summing and the relative errors are within ±11.4% in the rotor. For simplification, the CHILs in rotor will be still calculated by summing the losses generated by $\boldsymbol{U_d}^h$ and $\boldsymbol{U_q}^h$ independently due to the following three reasons. Firstly, the CHILs in the rotor are much smaller than those in the stator and take part <21.2% in the total loss. A total of ±11.4% error in the rotor will only result in ±2.4% error of the total CHIL. Secondly, the amplitudes of $\boldsymbol{U_d}^h$ and $\boldsymbol{U_q}^h$ in real applications usually differ a lot, for example at working condition A2, as shown in Fig. 5*a*. In these cases, such as cases 13 and 14 of Table 8, the relative errors are smaller than those in the cases where $\boldsymbol{U_d}^h$ and $\boldsymbol{U_q}^h$ have the same amplitude. Thirdly, according to Table 8, when the phase differences between $\boldsymbol{U_d}^h$ and $\boldsymbol{U_q}^h$ are obtuse angles, the losses obtained with independently summing are larger than those directly obtained from THFEA. Meanwhile, when the phase differences are acute angles, the losses obtained with independently summing are smaller than those directly obtained from THFEA. According to Fig. 5*b*, some phase differences are obtuse angles and some are acute angles. Hence, the relative error of the total CHIL can be further reduced by summing the losses caused by all harmonic components.

Fig. 9 summarises the procedure to calculate the total CHIL caused by all PWM voltage harmonics.

Table 4 compares the iron losses calculated with different methods. The CHIL obtained from the TSFEA method is calculated by subtracting the iron loss obtained under SVS excitation having 4032 steps in one electrical period from that calculated under PWM voltage excitation having 4032 steps in one electrical period. It can be seen that the major iron loss brought by PWM VSI is the eddy current loss and the increase of the hysteresis loss is limited [9]. The total CHIL calculated from the

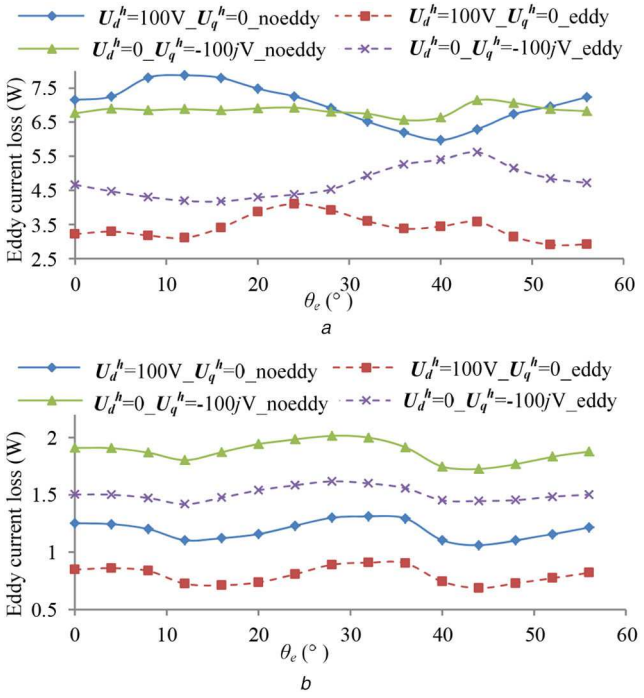

Fig. 10 *CHILs calculated with different methods under U_d^h or U_q^h excitation when f_h is 10 kHz*

(a) Stator, ***(b)*** Rotor

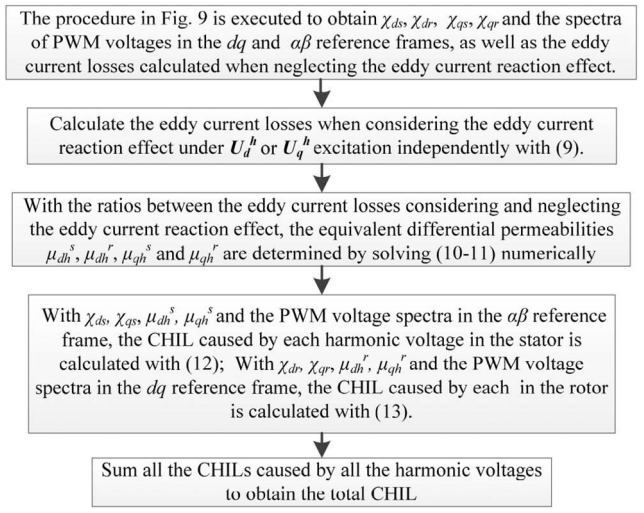

Fig. 11 *Calculation of the total CHIL at a given working condition when considering the eddy current reaction effect*

analytical method is close to that obtained from TSFEA and the relative error is within 1.3%. The iron loss calculated with SCS supply is very close to that obtained under SVS supply. Hence, the iron loss under SCS supply and the total CHIL obtained analytically method can be considered as the total iron loss under PWM VSI supply at operating condition A2, with which the computation time is reduced by 14 times. The proposed method needs totally 30 steps of THFEA to identify χ_d^s, χ_d^r, χ_q^s, and χ_q^r considering the influence of θ_e, while the traditional method has 4032 steps of non-linear TSFEA.

2.4 Considering the eddy current reaction effect

It has been shown in [9, 10] and [19, 20] that the eddy current reaction effect in the ESSs will cause significant reduction of the eddy current loss coefficient with the increase of frequency. Besides, the hysteresis loss will increase because of the uneven distribution of the flux density along the thickness direction of the ESSs according to the numerical results shown in [10]. In the Appendix, analytical expressions for modelling the variations of eddy current and hysteresis loss coefficients with frequency are given, with which the procedure to calculate the CHILs considering eddy current reaction effect is shown as follows:

(i) The decrease of the eddy current loss and the increase of the hysteresis loss can be modelled with (32) and (34), respectively, on the condition that the permeability of the ESSs in each element is known. Because the flux density variations caused by the PWM voltage harmonics are very small, the differential reluctivity tensor has been constructed for linearising the model [13], which is, however, inconvenient to use in (32) and (34). Hence, the scalar differential permeability μ_{sd} is still used in the analytical iron loss model [13, 18, 21].

Then, the eddy current loss caused by $\boldsymbol{U_d}^{\mathrm{h}}$ or $\boldsymbol{U_q}^{\mathrm{h}}$ considering the eddy current reaction effect in the ESSs can be calculated with the flux density obtained from THFEA as:

$$P_{\mathrm{eddy}}^{\mathrm{h\_c}} = \int_{\mathrm{Iron}} k_{\mathrm{e}} \cdot k_{\mathrm{fe}}(f_{\mathrm{h}}, \mu_{sd}) \cdot f_{\mathrm{h}}^2 \cdot \left(B_{\mathrm{r,r}}^2 + B_{\mathrm{r,i}}^2 + B_{\theta,\mathrm{r}}^2 + B_{\theta,\mathrm{i}}^2\right) \cdot \mathrm{d}v \quad (9)$$

Fig. 10 compares the eddy current losses calculated when considering and neglecting the eddy reaction effect in the stator and the rotor. Comparing with that calculated with (3) neglecting the reaction effect, the eddy current loss decreases significantly when calculated with (9) considering the reaction effect.

(ii) Because the differential permeability in each element of the ESSs often varies, the decrease of the eddy current loss with frequency varies significantly in each element. If the eddy current loss caused by each component of the PWM harmonics is calculated by summing up the contribution of each element, it will also be very time-consuming. Hence, the equivalent differential permeabilities of the stator and rotor under different harmonic excitations are proposed for fast calculating the iron losses considering the eddy current reaction effect directly. The equivalent differential permeablities are obtained by solving the following equations numerically, which are shown as:

$$k_{\mathrm{fe}}(f_{\mathrm{h}}, \mu_{d\mathrm{h}}^{\mathrm{s}}) = Pe_{d\mathrm{h}}^{\mathrm{s}}/Pn_{d\mathrm{h}}^{\mathrm{s}}, \quad k_{\mathrm{fe}}(f_{\mathrm{h}}, \mu_{q\mathrm{h}}^{\mathrm{s}}) = Pe_{q\mathrm{h}}^{\mathrm{s}}/Pn_{q\mathrm{h}}^{\mathrm{s}} \quad (10)$$

$$k_{\mathrm{fe}}(f_{\mathrm{h}}, \mu_{d\mathrm{h}}^{\mathrm{r}}) = Pe_{d\mathrm{h}}^{\mathrm{r}}/Pn_{d\mathrm{h}}^{\mathrm{r}}, \quad k_{\mathrm{fe}}(f_{\mathrm{h}}, \mu_{q\mathrm{h}}^{\mathrm{r}}) = Pe_{q\mathrm{h}}^{\mathrm{r}}/Pn_{q\mathrm{h}}^{\mathrm{r}} \quad (11)$$

where $Pe_{d\mathrm{h}}^{\mathrm{s}}$ is the eddy current loss in the stator obtained from (9) considering eddy reaction effect under $\boldsymbol{U_d}^{\mathrm{h}}$ excitation independently, while $Pn_{d\mathrm{h}}^{\mathrm{s}}$ is the eddy current loss in the stator obtained from (3) neglecting eddy reaction effect with the same excitation. f_{h} is suggested to be $2f_{\mathrm{c}}$ because most of CHILs are generated by components whose frequencies are close to $2f_{\mathrm{c}}$. $Pe_{q\mathrm{h}}^{\mathrm{s}}$ and $Pn_{q\mathrm{h}}^{\mathrm{s}}$ are the eddy current losses considering and neglecting the eddy reaction effect, respectively, under $\boldsymbol{U_d}^{\mathrm{h}}$ excitation independently. $Pe_{d\mathrm{h}}^{\mathrm{r}}$, $Pn_{d\mathrm{h}}^{\mathrm{r}}$, $Pe_{q\mathrm{h}}^{\mathrm{r}}$, and $Pn_{q\mathrm{h}}^{\mathrm{r}}$ are the corresponding eddy current losses in the rotor. $\mu_{d\mathrm{h}}^{\mathrm{s}}$ and $\mu_{d\mathrm{h}}^{\mathrm{r}}$ are the equivalent permeabilities under $\boldsymbol{U_d}^{\mathrm{h}}$ excitation in the stator and the rotor, respectively, while $\mu_{q\mathrm{h}}^{\mathrm{s}}$ and $\mu_{q\mathrm{h}}^{\mathrm{r}}$ are the equivalent permeabilities under $\boldsymbol{U_q}^{\mathrm{h}}$ excitation. The four parameters can be obtained by solving the equations shown in (10) and (11) with non-linear fitting. $\mu_{d\mathrm{h}}^{\mathrm{s}}$, $\mu_{d\mathrm{h}}^{\mathrm{r}}$, $\mu_{q\mathrm{h}}^{\mathrm{s}}$ and $\mu_{q\mathrm{h}}^{\mathrm{r}}$ at operating condition A2 are shown in Table 7, where μ_0 is the permeability in the vacuum.

(iii) After obtaining the equivalent permeabilities, the iron losses caused by the mth order harmonic voltage in the stator and the rotor when considering the eddy current reaction effect are calculated by the following equations, respectively:

$$\begin{aligned} P_m^{\mathrm{s\_c}} = {} & P_{m,\mathrm{e}}^{\mathrm{s},\alpha} \cdot k_{\mathrm{fe}}\left(f_m^{\alpha\beta}, \mu_{d\mathrm{h}}^{\mathrm{s}}\right) + P_{m,\mathrm{h}}^{\mathrm{s},\alpha} \cdot k_{\mathrm{fh}}\left(f_m^{\alpha\beta}, \mu_{d\mathrm{h}}^{\mathrm{s}}\right) \\ & + P_{m,\mathrm{e}}^{\mathrm{s},\beta} \cdot k_{\mathrm{fe}}\left(f_m^{\alpha\beta}, \mu_{q\mathrm{h}}^{\mathrm{s}}\right) + P_{m,\mathrm{h}}^{\mathrm{s},\beta} \cdot k_{\mathrm{fh}}\left(f_m^{\alpha\beta}, \mu_{q\mathrm{h}}^{\mathrm{s}}\right) \end{aligned} \quad (12)$$

$$P_m^{\mathrm{r\_c}} = P_{m,\mathrm{e}}^{\mathrm{r},d} \cdot k_{\mathrm{fe}}\left(f_m^{dq}, \mu_{d\mathrm{h}}^{\mathrm{r}}\right) + P_{m,\mathrm{h}}^{\mathrm{r},d} \cdot k_{\mathrm{fh}}\left(f_m^{dq}, \mu_{d\mathrm{h}}^{\mathrm{r}}\right) + P_{m,\mathrm{e}}^{\mathrm{r},q} \cdot k_{\mathrm{fe}}\left(f_m^{dq}, \mu_{q\mathrm{h}}^{\mathrm{r}}\right) + P_{m,\mathrm{h}}^{\mathrm{r},q} \cdot k_{\mathrm{fh}}\left(f_m^{dq}, \mu_{q\mathrm{h}}^{\mathrm{r}}\right) \quad (13)$$

(iv) The procedure to compute the total CHIL when considering the eddy current reaction effect is summarised in Fig. 11.

Table 9 compares the iron losses calculated with different methods considering the eddy reaction effect. The method in [10] is used for the TSFEA to compute the iron loss considering the eddy current reaction effect. The CHIL obtained from the TSFEA method is calculated by subtracting the iron loss obtained under SVS excitation having 4032 steps in one electrical period from that calculated under PWM voltage excitation having 4032 steps in one electrical period. The relative error between the total CHIL calculated with FEA and that calculated by the analytical method is within 2.1%. In addition, the CHIL calculated when considering the eddy reaction effect in the ESSs is significantly smaller than that neglecting this effect as shown in Table 4 [10]. The computation time with the analytical method is reduced by over 19 times.

3 Fast calculation of the total CHIL map

The procedure shown in Section 2 can be repeated for calculating the eight parameters at any working condition. Table 7 shows the parameters at six operating conditions in Fig. 1. In general, the eddy current loss factors for the stator increases with the fundamental currents, while those for the rotor decrease with the currents. Quadratic polynomials are proposed to fit the relationships between these parameters and load currents, which are shown as:

$$f(I_m, \alpha) = q_1 I_m^2 + q_2 I_m + q_3 I_m \alpha + q_4 \alpha^2 + q_5 \alpha + q_6 \quad (14)$$

$$I_m = \sqrt{i_{d0}^2 + i_{q0}^2}, \quad \alpha = -\arcsin(i_{d0}/I_m) \quad (15)$$

where f can be χ_d^{s}, χ_d^{r}, χ_q^{s}, χ_q^{r}, $\mu_{d\mathrm{h}}^{\mathrm{s}}$, $\mu_{d\mathrm{h}}^{\mathrm{r}}$, $\mu_{q\mathrm{h}}^{\mathrm{s}}$ or $\mu_{q\mathrm{h}}^{\mathrm{r}}$. Coefficients from q_1 to q_6 can be fitted with the parameters given in Table 7. Then the parameters at other operating conditions can be obtained directly with the fitted coefficients using (14).

To verify the fitting effect, the eight parameters calculated with THFEA are compared with those directly obtained from the fitted quadratic polynomials at four other working conditions from T1 to T4, as shown in Table 10. For χ_d^{s} and χ_q^{s}, the calculated and the fitted agree with each other very well and the relative errors between them are within 4.2%. Although the relative errors for χ_d^{r} and χ_q^{r} are a little bit larger, especially at working condition T4, χ_d^{r} and χ_q^{r} themselves are rather small. Hence, they will not cause large errors in the total calculated CHILs, which will be demonstrated later.

The fitting errors of the equivalent differential permeabilities are larger than those of the eddy current loss factors, which are within 33.1% at the four working conditions. They will affect the total calculated CHILs when considering the eddy current reaction effect. However, fortunately, it will be shown later that the total calculated CHILs are not very sensitive to the errors in the fitted equivalent differential permeablities.

In Table 11, the CHILs calculated with the proposed method are compared with those obtained from the TSFEA at different operating conditions. The switching frequencies for A1, A2, and T4 are set to 4.8 kHz to ensure that the carrier ratio is an integer, while the switching frequencies for all other working conditions are set to 5 kHz. When calculating the iron losses under PWM VSI supply, there are 112 steps TSFEA in each carrier cycle to make sure the preponderant harmonic voltages generated by PWM can be distinguished. Hence, there are 4032 steps in one electrical period at A1 and A2, 8400 steps at A5 and T1, 2800 steps at T2, 1680 steps at T3, and 1008 steps at T4. Short time steps are also used when calculating the iron losses under SVS supply and the step number in one electrical period is set to be the same as that under PWM VSI supply at each working condition for a fair comparison. The CHIL calculated with the TSFEA is considered as the difference between iron losses calculated using PWM VSI and SVS excitations. When generating the PWM waveform numerically, the given modulation ratio and phase angle have been carefully turned to make the fundamental component in the generated PWM waveform as close as possible to the sinusoidal voltage applied for calculating the iron loss under SVS supply at each working condition. In addition, the iron losses calculated with the TSFEA using SCS excitations are also shown for comparison. Short time steps are not used and there are fixed 144 steps in one

Table 9 Comparison of iron losses calculated with different methods when considering the eddy current reaction effect

Method		Time, min	Eddy current loss, W		Hysteresis loss, W	
			Stator	Rotor	Stator	Rotor
TS_SCS_144		5.4	59.2	11.0	81.1	1.8
TS_SCS_4032		196.4	~~63.8~~	12.0	81.6	1.8
TS_SVS_144		5.3	58.5	10.7	80.6	1.7
TS_SVS_4032		182.0	59.4	11.6	80.9	1.7
TS_PWM_4032		184.5	98.2	20.5	86.1	2.6
TSFEA	CHIL	—	38.8	8.9	5.1	0.9
Proposed	CHIL	4.1	40.0	9.8	4.3	0.7

Table 10 Fitting errors of the eight parameters at four arbitrarily chosen working conditions from T1 to T4

	χ_d^{s}, 10^{-4}W/V^2			χ_d^{r}, 10^{-4}W/V^2			χ_q^{s}, 10^{-4}W/V^2			χ_q^{r}, 10^{-4}W/V^2		
	THFEA	Fitted	Error, %	THFEA	Fitted	Error, %	THFEA	Fitted	Error	THFEA	Fitted	Error, %
T1	6.95	7.23	4.0	1.13	1.06	−6.6	7.58	7.45	−1.7%	1.87	1.75	−6.4
T2	6.67	6.74	1.1	1.29	1.34	4.2	6.48	6.21	−4.2%	1.98	2.11	6.3
T3	6.33	6.27	−0.8	1.17	1.28	9.8	5.90	5.68	−3.6%	2.37	2.39	0.8
T4	6.33	6.24	−1.5	0.71	0.87	21.2	5.77	5.60	−2.9%	2.09	2.19	4.9
		$\mu_{d\mathrm{h}}^{\mathrm{s}}/\mu_0$			$\mu_{d\mathrm{h}}^{\mathrm{r}}/\mu_0$			$\mu_{q\mathrm{h}}^{\mathrm{s}}/\mu_0$			$\mu_{q\mathrm{h}}^{\mathrm{r}}/\mu_0$	
	THFEA	Fitted	Error, %	THFEA	Fitted	Error, %	THFEA	Fitted	Error	THFEA	Fitted	Error, %
T1	2358	2285	−3.1	1442	1326	−8.1	1356	1014	−25.2%	932	873	−6.3
T2	3506	3332	−5.0	1517	1672	10.3	1846	2003	8.5%	1088	1139	4.7
T3	6162	4754	−22.9	2666	2139	−19.8	3994	2826	−29.2%	2437	1630	−33.1
T4	7660	6122	−20.1	3028	2939	−2.9	6039	4730	−21.7%	4519	3792	−16.1

Table 11 Verification of the CHILs calculated with the proposed method at different operating conditions

Speed, r/min		Neglecting eddy current reaction effect						Considering eddy current reaction effect					
		Iron loss with TSFEA, W			Proposed, W			Iron loss with TSFEA, W			Proposed, W		
		SCS _144	SVS _short	PWM _short	**CHIL**	**THFEA**	**Fitted**	SCS _144	SVS _short	PWM _short	**CHIL**	**THFEA**	**Fitted**
A1	2000	230.2	232.6	335.0	**102.4**	**104.0**	**104.0**	231.0	231.2	298.2	**67.0**	**67.9**	**67.9**
A2	2000	153.6	152.6	249.1	**96.5**	**95.3**	**95.3**	153.1	153.7	207.3	**53.6**	**54.7**	**54.7**
A5	1000	34.0	34.2	84.1	**50.0**	**51.0**	**51.0**	34.1	34.2	51.7	**17.5**	**20.2**	**20.2**
T1	1000	71.3	72.5	145.6	**73.0**	**73.2**	**73.1**	71.2	71.2	108.0	**36.8**	**38.7**	**41.1**
T2	3000	217.2	215.7	310.1	**94.4**	**93.4**	**93.2**	216.1	218.6	266.5	**47.9**	**49.4**	**48.7**
T3	5000	425.3	418.7	497.9	**79.2**	**75.4**	**74.8**	412.9	421.7	456.8	**35.1**	**33.2**	**36.4**
T4	8000	1019.9	1002.0	1085.8	**83.7**	**78.3**	**78.2**	899.7	933.2	960.6	**27.4**	**32.8**	**34.7**

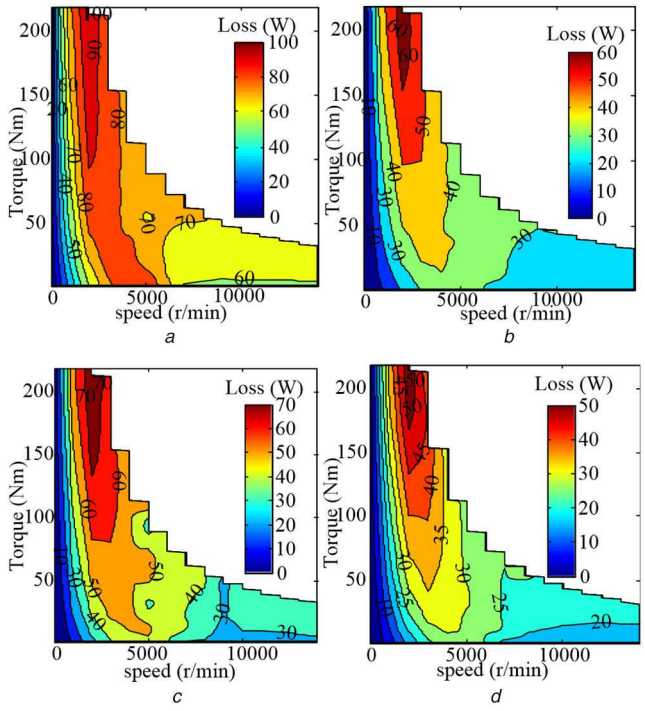

Fig. 12 *CHIL maps over the entire operating range*
(a) f_c = 5 kHz_no eddy, ***(b)*** f_c = 5 kHz_eddy, ***(c)*** f_c = 3 kHz_eddy, ***(d)*** f_c = 8 kHz_eddy

electrical period at each working condition under the SCS supply because it is found that large numerical errors may happen at some working conditions (A2, T2 and T4) due to the short-term analysis under SCS supplies. However, fortunately, the numerical errors due to the short-term analysis are limited in the TSFEA using PWM VSI and SVS excitations. The iron losses under SCS supply are very close to those obtained under SVS supply when the speed is not too high. However, as the speed going high, the iron loss caused by low order harmonic currents becomes non-negligible [13] and makes the iron losses calculated with the two methods different. Accurate calculation of low order harmonics currents and its influence on iron losses may need the co-simulation of IPMSMs, inverters, and controllers, which is not the topic of this paper. The eight parameters obtained directly from the THFEA and the quadratic polynomials are used respectively for calculating the CHILs to testify the fitting effect.

It can be seen from Table 11 that when the eddy current reaction effect is neglected, the CHILs obtained with the proposed method agree very well with those calculated with the TSFEA. The relative errors are within 6.6% at the seven working conditions and within 2.2% at the working conditions whose speeds are below 3000 r/min.

When the eddy current reaction effect is considered, the relative errors become a little bit larger, which are still within 16% at working conditions whose speeds are below 5000 r/min. This may be because the CHILs themselves are smaller when considering the eddy current reaction, and they are obtained with the difference between two larger numbers where numerical errors may become more obvious. Besides, when the eddy current reaction effect is considered with the proposed analytical method, the scalar differential permeability had to be used which may cause some errors. At working condition T4, the relative error of the CHIL may reach to 26.7%, however, the CHIL is only a small proportion of the total iron loss at high speed, which will affect little on the accuracy of the total iron loss calculation. If the total iron losses under PWM VSI supply are calculated with the sum of the losses under SVS supply and the CHILs obtained with the proposed method, the relative errors between the total losses and those calculated with direct TSFEA under PWM VSI supplies are within 5.3% at the seven working conditions no matter whether the eddy current reaction effect is considered or not.

When neglecting the eddy current reaction effect, the relative errors between the CHILs calculated with the parameters from THFEA and those calculated with the fitted parameters are within 0.8% at working conditions from T1 to T4, which demonstrates the accuracy of the polynomial fitting for calculating the CHILs at arbitrary working conditions when the eddy current reaction effect is neglected. However, when it is considered, the relative errors between the calculated and the fitted become larger because the fitting errors of the equivalent differential permeabilities according to Table 10. Even so, the calculated CHILs from THFEA and those calculated with the fitted parameters are still within 9.6% at the four working conditions when the eddy current reaction effect is considered, which shows that the proposed method is still an effective way for fast estimating CHILs at arbitrary working conditions.

With the polynomial shown in (14) and the PWM voltage spectra of each operating condition obtained from the double Fourier integral method shown in [13, 17], the CHIL map over the entire operation range can be obtained as shown in Fig. 12. Figs. 12*a* and *b* show that the CHILs calculated when considering the eddy reaction effect in the ESSs is significantly smaller than those obtained when neglecting the eddy reaction effect. The influence of the switching frequency on the iron loss can be investigated with the proposed method as shown in Figs. 12*c* and *d*. With the increase of the switching frequency, for example in the application with next generation power semiconductors, the calculation time with time-stepping FEA will further increase and the merits of the proposed method will become more obvious. It takes only about an hour to obtain each map shown in Fig. 12 with 177 operating points.

4 Experimental verification

4.1 Experimental setup

The iron loss model using the 1D non-linear TSFEA was claimed to be verified with Fig. 16 of [10]. However, according to Fig. 2 of [3], the 1D TSFEA method considering the eddy current reaction effect gave results smaller than the measured ones. Considering the difficulty to accurately separate the CHILs with the experiment on electrical machines, we measured and calculated the iron losses of a specimen under PWM VSI supply to testify the iron loss model using the 1D non-linear TSFEA and the proposed method considering the eddy current reaction effect. The specimen, consisting of ESSs and copper windings, is shown Fig. 13. The ESSs have a thickness of 0.35 mm and there are 50 sheets in the

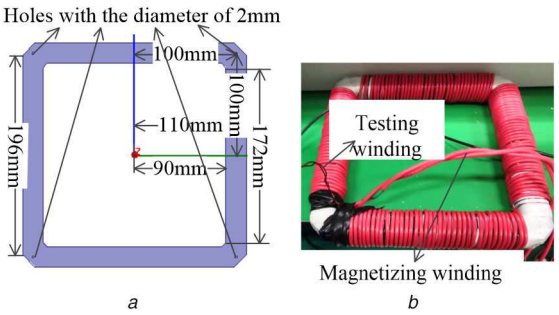

Fig. 13 *Specimen for iron loss measurement*
(a) Dimension of the laminated core, ***(b)*** Picture

Table 12 Loss coefficients of the specimen at low frequency

k_e, W/m^3/Hz^2/T^2	0.62896
k_{h0}, W/m^3/Hz/T^2	310.362
k_{h1}, W/m^3/Hz/T^3	−270.622
k_{h2}, W/m^3/Hz/T^4	111.978

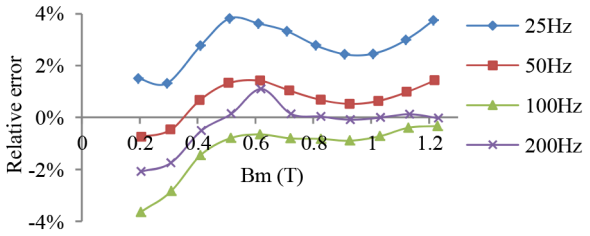

Fig. 14 *Relative errors between calculated and measured iron losses under SVS source supply at low frequencies*

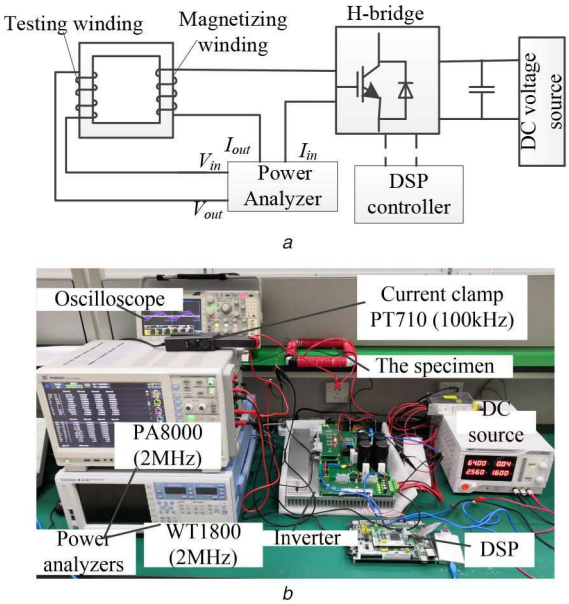

Fig. 15 *Measuring iron loss under PWM VSI supply*
(a) Diagram, ***(b)*** Picture

specimen. The magnetising and testing windings have both 152 turns.

The iron losses under SVS supply are first measured to identify k_e and k_h at low frequency with the traditional open-loop Epstein frame test method [22]. The amplitudes of measured flux densities are limited within 1.2 T to avoid the waveform distortion at the saturation region due to the voltage drop on the resistance of the magnetising winding [23], which guarantees the measured loss is generated by the purely sinusoidal flux density waveform. Then, to ensure that the iron losses generated by the low-frequency

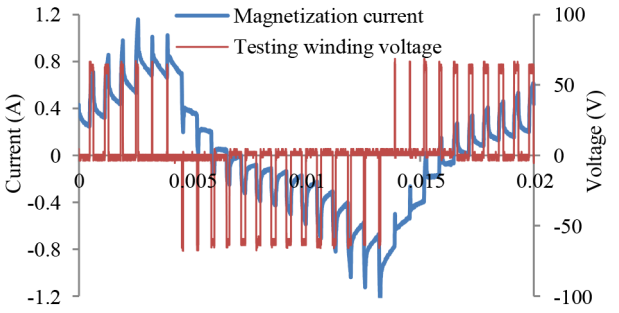

Fig. 16 *Measured current and voltage when m is 0.3, f_o is 50 Hz, and f_c is 750 Hz*

sinusoidal flux density variations can be calculated accurately, the iron loss model with variable coefficients is used to fit the measured losses [19, 20] at frequencies ranging from 25 to 200 Hz, which is shown as follows:

$$p_{\text{iron}} = k_e \cdot f^2 B_m^2 + k_h(B_m) \cdot f B_m^2$$
$$k_h(B_m) = k_{h0} + k_{h1} B_m + k_{h2} \cdot (B_m)^2 \tag{16}$$

where B_m is the amplitude of the flux density variation, and p_{iron} is the iron loss density. The eddy current loss coefficient is assumed as constant, while the hysteresis loss coefficient varies with B_m. k_e, k_{h0}, k_{h1}, and k_{h2} are constants to be fitted, which are shown in Table 12. Fig. 14 shows the relative errors between the iron losses calculated with the coefficients shown in Table 12 and the measured ones, which ensures that the iron losses caused by the low-frequency fundamental component can be computed accurately.

The iron losses under PWM VSI supply are then measured with the experimental setup shown in Fig. 15. Two 2 MHz power analysers, WT1800 and PA8000, are used separately to measure the iron loss to ensure the measured results are accurate. The voltage of the DC source is set to be constant as 64 V. Fig. 16 shows the measured magnetisation current and test winding voltage when the modulation ratio m is 0.3, the carrier frequency f_c is 750 Hz, and the fundamental frequency f_o is 50 Hz. The high-frequency components over 50 kHz in the measured current have been filtered.

4.2 Results comparison

Because the specimen has simple structure, the flux density variation at anywhere of the ESSs can be considered as the same and calculated analytically with the spectral of the testing winding voltage as:

$$B_m^n = \frac{U_m^n}{2\pi f_n N_2 S} \tag{17}$$

where U_m^n and f_n are amplitude and frequency of nth harmonic in the measured voltage of the test winding, respectively. $B_m^n$is the amplitude of the nth harmonic of the flux density. N_2 is the turn number of the testing winding and S is cross section area of the ESSs.

When the eddy current reaction effect is neglected, the total iron loss density can be calculated as:

$$p_i^n = p_i^1 + p_i^{h\_n}$$
$$p_i^1 = k_e \cdot \left(f_1 B_m^1\right)^2 + k_h\left(B_m^1\right) \cdot f_1 \left(B_m^1\right)^2$$
$$p_i^{h\_n} = k_e \cdot \sum_{n=2}^{+\infty} \left(f_n B_m^n\right)^2 + \sum_{n=2}^{+\infty} k_h(B_m^n) \cdot f_n (B_m^n)^2 \tag{18}$$

where p_i^1 is the iron loss density generated by the fundamental component and $p_i^{h\_n}$ is the CHIL density.

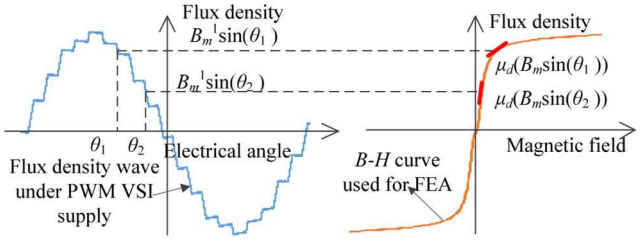

Fig. 17 *Differential permeability variation with flux density*

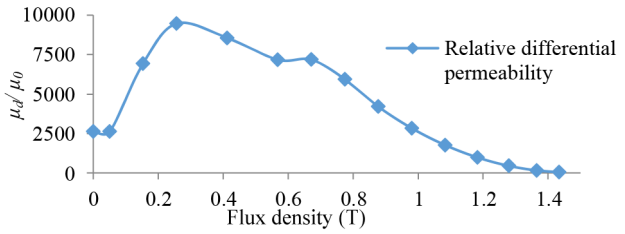

Fig. 18 *Relative differential permeability obtained from the B-H curve of the silicon steel sheet in the specimen*

To calculate the iron loss considering the eddy current eddy with the proposed method shown in Section 2.4, the equivalent differential permeability has to be determined. As shown in Fig. 17, due to the variation of the fundamental flux density with time or the electrical angle, the differential permeability also varies, which is similar to the case in the IPMSM where the differential permeability varies with the rotor position. The equivalent differential permeability μ_d^{e} can be calculated by solving the following equation numerically as:

$$k_{\mathrm{fe}}(f_{\mathrm{h}},\mu_{\mathrm{d}}^{\mathrm{e}})=\frac{2}{\pi}\int_0^{\pi/2}k_{\mathrm{fe}}\left(f_{\mathrm{h}},\mu_{\mathrm{d}}\left(B_m^1\cdot\sin(\theta)\right)\right)\cdot\mathrm{d}\theta \tag{19}$$

where the differential permeability μ_{d} is the function of the flux density, as shown in Fig. 18, which can be calculated with the *B-H* curve for the traditional FEA. f_{h} is set to be twice of f_{c}.

The conductivity of the silicon steel can be calculated with (30), and then the total iron loss density considering the eddy current effect is calculated as:

$$\begin{aligned}p_i^{\mathrm{c\_}BH}&=p_i^1+p_i^{\mathrm{h\_}BH}\\ p_i^{\mathrm{h\_}BH}&=k_{\mathrm{e}}\cdot\sum_{n=2}^{+\infty}k_{\mathrm{fe}}(f_n,\mu_d^{\mathrm{e}})\cdot(f_nB_m^n)^2\\&\quad+\sum_{n=2}^{+\infty}k_{\mathrm{h}}(B_m^n)\cdot k_{\mathrm{fh}}(f_n,\mu_{\mathrm{d}}^{\mathrm{e}})\cdot f_n\cdot(B_m^n)^2\end{aligned} \tag{20}$$

where $p_i^{\mathrm{h\_}BH}$ is the CHIL density considering the eddy current effect with the traditional *B-H* curve.

Fig. 19 compares the iron loss densities calculated with different methods at different working conditions. When f_{o} is 200 Hz, the iron losses are also calculated with the TSFEA method in [10] for a comparison. During the TSFEA, the time step is set to be 2×10^{-6} s and there 2500 steps in one electrical period. Some conclusions can be drawn with the comparison. First, the iron loss under PWM VSI supply will be significantly overestimated when the iron loss coefficients at low frequency are used to calculate the CHILs and the eddy current reaction effect is neglected. The maximum relative error reaches 37% at Fig. 19*a* when f_{c} is 15 kHz. Secondly, when only the loss generated by the fundamental component is taken into account, the iron loss under PWM VSI excitation will be significantly underestimated, the maximum relative error reaches to −46% at Fig. 19*a* when f_{c} is 750 Hz. Thirdly, the iron loss densities calculated with the 1D non-linear TSFEA [10], p_i^{TSFEA}, are very close to $p_i^{\mathrm{c\_}BH}$, which further validates the accuracy of the proposed method. Besides, they are

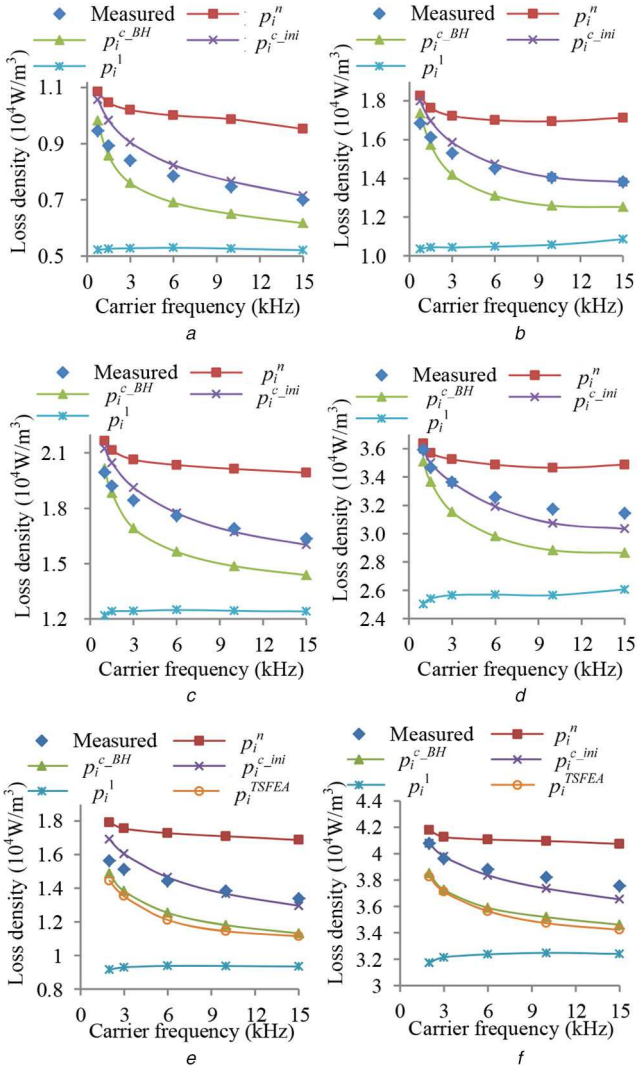

Fig. 19 *Comparison of the iron loss densities calculated with different methods under PWM VSI supply*
(a) f_{o} = 50 Hz_m = 0.2, ***(b)*** f_{o} = 50 Hz_m = 0.3, ***(c)*** f_{o} = 100 Hz_m = 0.4, ***(d)*** f_{o} = 100 Hz_m = 0.6, ***(e)*** f_{o} = 200 Hz_m = 0.4, ***(f)*** f_{o} = 200Hz_m = 0.8

close to the measured ones when f_{c} is low (below 3 kHz). However, when the f_{c} is high, the relative errors between $p_i^{\mathrm{c\_}BH}$ and the measured ones reach a maximum value of −15% at Fig. 19*e* when f_{c} is 15 kHz. This experimental result is in accordance with Fig. 2 of [3], where the 1D TSFEA method is reported to underestimate the iron loss.

4.3 Error discussion and modification

According to the discussion in the last subsection, the proposed method considering the eddy current effect and the method in [10] underestimate the iron losses under PWM VSI supply when f_{c} is high. After deeply investigating the real magnetisation progress of the ESSs, the cause of the error is found. The error is because the *B-H* curve for traditional FEA is not able to reflect the real relationship between the magnetic field and the flux density in ESSs. The hysteresis characteristic is obvious especially when the ESSs are not saturated [24, 25].

Fig. 20 shows the measured hysteresis loops at different carrier frequencies when f_{o} is 50 Hz and *m* is 0.2. It can be seen that when a PWM voltage pulse is suddenly applied, the increasing rate of the flux density is not a constant. It first increases at a rate of the differential permeability μ_{d}^1, which is close to the initial permeability of the silicon steel [24]. Then, the flux density increases at a rate of μ_{d}^2, which is close to the differential permeability obtained from the *B-H* curve for traditional FEA

shown in Figs. 17 and 18. When the PWM voltage pulse disappears, the flux density decreases at a rate of $\mu_d{}^3$, which is close to $\mu_d{}^1$. This reveals that it is very difficult to accurately model the differential permeability with only the *B-H* curve for traditional FEA. When f_c or the carrier ratio is low, the equivalent differential permeability is close to that shown in Fig. 18, which makes $p_i^{c\_BH}$ close to the measured loss density at low carrier frequency. However, with the increase of f_c, the equivalent differential permeability becomes lower and closer to the initial permeability of the ESSs, which reduces the eddy current reaction effect and makes $p_i^{c\_BH}$ lower than the measured loss density.

To measure the initial permeability of the silicon steel, small flux density variation with low frequency needs to be generated in the specimen, which needs a small SVS with low frequency as the excitation source. Fig. 21 shows the proposed system for measuring the initial permeability of the silicon steel, where the LCR meter with adjustable output voltage not only serves as the SVS but also gives the inductance of the specimen, with which the initial permeability can be computed as:

$$\mu_{\text{ini}} = \frac{L_m \cdot l_{\text{eq}}}{N_2^2 S} \tag{21}$$

where L_m is the measured inductance. l_{eq} is the equivalent length of the magnetic path.

Sinusoidal voltages ranging from 5 to 1000 mV are generated by the LCR meter and applied in the magnetising winding. Then the voltage in the test winding is measured with the millivoltmeter to compute the amplitude of the flux density variation, which is shown as:

$$B_m^{\text{ini}} = \frac{V_{\text{test}}}{\sqrt{2}\pi f_{\text{test}} N_2 S} \tag{22}$$

where V_{test} is the RMS value of the test winding voltage. f_{test} is the frequency of the voltage generated by the LCR meter, which is chosen as 50 Hz here. It is found that B_m^{ini} has significant influence on μ_{ini} and their relationship is shown in Fig. 22.

When the equivalent differential permeability is considered as μ_{ini} and calculated with $B_m{}^n$ according to the relationship in Fig. 22, the iron loss density considering the eddy current reaction effect can be computed with:

$$\begin{aligned} p_i^{c\_\text{ini}} &= p_i^1 + p_i^{h\_\text{ini}} \\ p_i^{h\_\text{ini}} &= k_e \cdot \sum_{n=2}^{+\infty} k_{\text{fe}}(f_n, \mu_{\text{ini}}(B_m^n)) \cdot (f_n B_m^n)^2 \\ &\quad + \sum_{n=2}^{+\infty} k_h(B_m^n) \cdot k_{\text{fh}}(f_n, \mu_{\text{ini}}(B_m^n)) \cdot f_n \cdot (B_m^n)^2 \end{aligned} \tag{23}$$

where $p_i^{h\_BH}$ is the CHIL density considering the eddy current effect with the initial differential permeability.

$p_i^{c\_\text{ini}}$ is also shown in Fig. 19 for comparison. It can be seen that although the excess loss is neglected, $p_i^{c\_\text{ini}}$ agrees very well with the measured loss density and the relative errors are within 4% when f_c is over 3 kHz. However, when f_c is below 3 kHz, $p_i^{c\_\text{ini}}$ tend to overestimate the iron loss and the maximum relative error reaches to 12% at Fig. 19*a*, which is because the differential permeability is closer to that obtained from the traditional *B-H* curve but not the initial permeability when f_c is low.

Because the method in [10] uses the traditional *B-H* curve to model the silicon steel, the differential permeability is overestimated leading to the underestimation of the iron loss density when f_c is high. The proposed method can not only give results similar to that in [10] in a faster manner but also has the potential to be improved to give a more accurate result on condition that the equivalent differential permeability is accurately modelled, which is however rather difficult due to the complex hysteresis phenomenon.

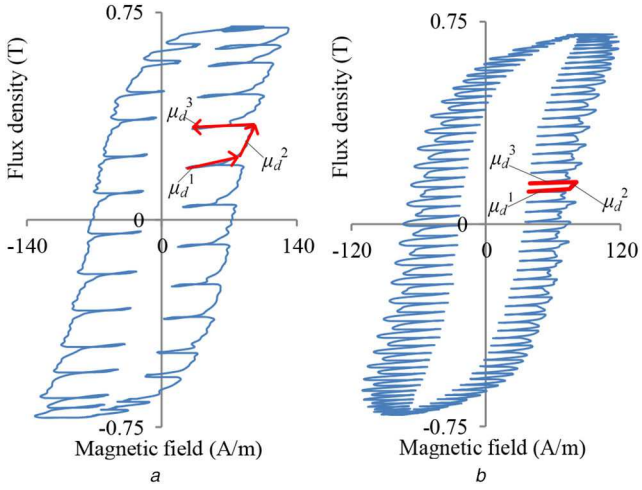

Fig. 20 *Hysteresis loops when f_o is 50 Hz and m is 0.2*
(a) f_c = 750 Hz, ***(b)*** f_c = 3 kHz

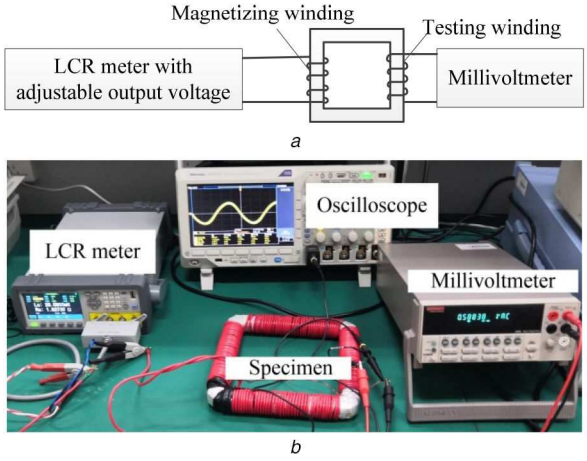

Fig. 21 *Measuring the initial permeability*
(a) Diagram, ***(b)*** Picture

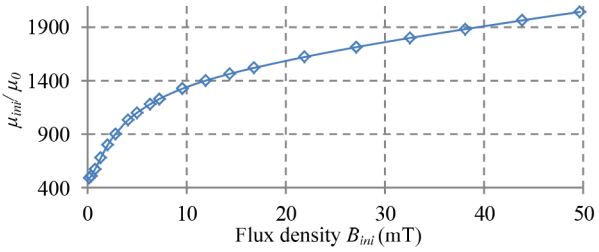

Fig. 22 *Variation of μ_{ini} with B_{ini}*

5 Conclusion

A method combining the FDRTM and the linear THFEA has been proposed for fast calculating the CHILs in IPMSMs. The influence of the eddy current reaction effect in the ESSs on the CHILs is modelled. Main contributions of this paper are summarised as follows:

(i) It is shown that the functional relationships between the harmonic voltages and corresponding CHILs can be fast investigated with the proposed method and modelled with simple expressions.
(ii) Comparing with the traditional TSFEA method for the CHIL calculation, the computational time of the proposed method reduces over ten times at one working condition and over hundreds

of times for calculating the CHIL map over the entire working range.

(iii) The proposed method agrees well with the traditional TSFEA especially when the eddy current effect is neglected. However, this effect needs to be considered for accurately calculating CHILs, and the accuracy depends on whether the differential permeability can be accurately modelled, which still needs further investigation in the future considering the hysteresis characteristic of ESSs.

6 Acknowledgments

This work was supported by the National Natural Science Foundation of China under project 51907053, by the Natural Science Foundation of Jiangsu Province of China under project BK20190489, and by the China Postdoctoral Science Foundation under grant no. 2019M661708.

7 References

[1] Burress, T. A.: 'Evaluation of the 2010 Toyota Prius hybrid synergy drive system', Oak Ridge Nat. Lab., Tech. Rep. ORNL/TM-2010/253, Oak Ridge, TN, USA, 2010

[2] Khayamy, M., Chaoui, H.: 'Efficient PMSM-inverter-based drive for vehicular transportation systems', *IEEE Trans. Transp. Electrific.*, 2018, **67**, (6), pp. 4783–4792

[3] Yamazaki, K., Togashi, Y., Ikemi, T., *et al.*: 'Reduction of inverter carrier harmonic losses in interior permanent magnet synchronous motors by optimizing rotor and stator shapes', *IEEE Trans. Ind. Appl.*, 2019, **55**, (1), pp. 306–315

[4] Balamurali, A., Feng, G., Lai, C., *et al.*: 'Maximum efficiency control of PMSM drives considering system losses using gradient descent algorithm based on DC power measurement', *IEEE Trans. Energy Conver.*, 2018, **33**, (4), pp. 2240–2249

[5] Dlala, E., Solveson, M., Stanton, S., *et al.*: 'Efficiency map simulations for an interior pm motor with experimental comparison and investigation of magnet size reduction'. Proc. Int. Conf. Electric Machines & Drives, Chicago, IL, USA, May 2013, pp. 23–29

[6] Chen, X., Wang, J., Sen, B., *et al.*: 'A high-fidelity and computationally efficient model for interior permanent-magnet machines considering the magnetic saturation, spatial harmonics, and iron loss effect', *IEEE Trans. Ind. Electron.*, 2015, **62**, (7), pp. 4044–4055

[7] Miyama, Y., Hazeyama, M., Hanioka, S., *et al.*: 'PWM carrier harmonic iron loss reduction technique of permanent-magnet motors for electric vehicles', *IEEE Trans. Ind. Appl.*, 2016, **52**, (4), pp. 2865–2871

[8] Yamazaki, K., Seto, Y.: 'Iron loss analysis of interior permanent-magnet synchronous motors-variation of main loss factors due to driving condition', *IEEE Trans. Ind. Appl.*, 2006, **42**, (4), pp. 1045–1052

[9] Gerlando, A.D., Perini, R.: 'Evaluation of the effects of the voltage harmonics on the extra iron losses in the inverter fed electromagnetic devices', *IEEE Trans. Energy Conver.*, 1999, **14**, (1), pp. 57–65

[10] Yamazaki, K., Fukushima, N.: 'Iron loss model for rotating machines using direct eddy current analysis in electrical steel sheets', *IEEE Trans. Energy Conver.*, 2010, **25**, (3), pp. 633–641

[11] Boglietti, A., Cavagnino, A., Lazzari, M., *et al.*: 'Predicting iron losses in soft magnetic materials with arbitrary voltage supply: an engineering approach', *IEEE Trans. Magn.*, 2003, **39**, (2), pp. 981–989

[12] Boglietti, A., Cavagnino, A., Ionel, D. M., *et al.*: 'A general model to predict the iron losses in PWM inverter-fed induction motors', *IEEE Trans. Ind. Appl.*, 2010, **46**, (5), pp. 1882–1890

[13] Zhu, S., Wang, H., Zhang, J., *et al.*: 'Fast calculation of carrier harmonic loss in permanent magnet of IPMSM under PWM VSI supply over entire working range', *IEEE Trans. Energy Conver.*, 2019, **34**, (3), pp. 1581–1592

[14] Alberti, L., Bianchi, N., Morandin, M., *et al.*: 'Finite-element analysis of electrical machines for sensorless drives with high-frequency signal injection', *IEEE Trans. Ind. Appl.*, 2014, **50**, (3), pp. 1871–1879

[15] Gyselinck, J., Dular, P., Sadowski, N., *et al.*: 'Incorporation of a Jiles–Atherton vector hysteresis model in 2D FE magnetic field computations: application of the Newton–Raphson method', *COMPEL, Int. J. Comput. Math. Electr. Electron. Eng.*, 2004, **23**, (3), pp. 685–693

[16] Tessarolo, A., Agnolet, F., Luise, F., *et al.*: 'Use of time-harmonic finite-element analysis to compute stator winding eddy-current losses due to rotor motion in surface permanent-magnet machines', *IEEE Trans. Energy Conver.*, 2012, **27**, (3), pp. 670–679

[17] Holmes, D., Lipo, T.: '*Pulse width modulation for power converters: principles and practice*' (Wiley & Sons, Canada, 2003), pp. 259–291

[18] Zhu, S., Cheng, M., Zhu, Y.: 'Fast calculation of PM eddy current loss in IPMSM under PWM VSI supply based on the spectra of line-line voltage', *IEEE Trans. Magn.*, 2018, **54**, (11), Article ID 18164420

[19] Ionel, D.M., Popescu, M., McGilp, M.I., *et al.*: 'Computation of core losses in electrical machines using improved models for laminated steel', *IEEE Trans. Ind. Appl.*, 2007, **43**, (6), pp. 1554–1564

[20] Popescu, M., Ionel, D. M., Boglietti, A., *et al.*: 'A general model for estimating the laminated steel losses under PWM voltage supply', *IEEE Trans. Ind. Appl.*, 2010, **46**, (4), pp. 1389–1396

[21] Yamazaki, K., Kanou, Y.: 'Rotor loss analysis of interior permanent magnet motors using combination of 2-D and 3-D finite element method', *IEEE Trans. Magn.*, 2009, **45**, (3), pp. 1772–1775

[22] Zhu, S., Cheng, M., Dong, J., *et al.*: 'Core loss analysis and calculation of stator permanent-magnet machine considering DC-biased magnetic induction', *IEEE Trans. Ind. Electron.*, 2014, **61**, (10), pp. 5203–5212

[23] Tekgun, B., Chowdhury, A. R. B., Mahmood, M. A., *et al.*: 'Design and implementation of a sinusoidal flux controller for core loss measurements'. IEEE Proc. Applied Power Electronics Conf. and Exposition, Long Beach, America, March 2016, pp. 207–214

[24] Jiles, D. C., Thoelke, J. B., Devine, M. K.: 'Numerical determination of hysteresis parameters for the modeling of magnetic properties using the theory of ferromagnetic hysteresis', *IEEE Trans. Magn.*, 1992, **28**, (1), pp. 27–35

[25] Chang, L., Lee, W., Jahns, T. M., *et al.*: 'Investigation and prediction of PWM-induced iron loss in lamination steels using high-frequency inverters with wide-bandgap switches'. IEEE Proc. Energy Conversion Congress and Exposition, Baltimore, America, September 2019, pp. 2307–2314

8 Appendix

Assuming that the ESSs have a constant permeability μ, the equation for the flux density distribution along the thickness direction of one ESS, as shown in Fig. 23, is written as:

$$\frac{\partial \boldsymbol{B}_y^2}{\partial x^2} = \mathrm{j} \cdot 2\pi f \mu \sigma \boldsymbol{B}_y^2, \quad \boldsymbol{B}_y\Big|_{x=\pm\frac{t}{2}} = \boldsymbol{B}_0 \tag{24}$$

where $\boldsymbol{B}_y$ is the flux density passing through the ESS. f is the frequency of the flux density variation and σ is the conductivity of the ESS. t is the thickness of the ESS. $\boldsymbol{B}_0$ is the flux density in the edge of the ESS.

Hence, $\boldsymbol{B}_y$ can be obtained by:

$$\boldsymbol{B}_y = \boldsymbol{B}_0 \frac{\cosh(\boldsymbol{k} \cdot x)}{\cosh(\boldsymbol{k} \cdot t/2)}, \quad \boldsymbol{k} = \frac{1+j}{\Delta}, \quad \Delta = \sqrt{\frac{1}{\pi f \mu \sigma}} \tag{25}$$

where Δ is the skin depth. The average flux density passing through the ESS (Fig. 23) is defined as:

$$\boldsymbol{B}_y^{\mathrm{av}} = \frac{1}{t}\int_{-t/2}^{t/2} \boldsymbol{B}_y \cdot \mathrm{d}x = \frac{2\boldsymbol{B}_0}{t \cdot \boldsymbol{k}} \frac{\sinh(t \cdot \boldsymbol{k}/2)}{\mathrm{cosv}(t \cdot \boldsymbol{k}/2)} \tag{26}$$

Hence, the relationship between $\boldsymbol{B}_y$ and $\boldsymbol{B}_y^{\mathrm{av}}$ can be shown as:

$$\boldsymbol{B}_y = \boldsymbol{B}_y^{\mathrm{av}} \frac{\cosh(\boldsymbol{k} \cdot x)}{\sinh(\boldsymbol{k} \cdot t/2)} \cdot \frac{\boldsymbol{k}t}{2} \tag{27}$$

The classical eddy current loss density considering the uneven eddy current distribution in the ESS can be calculated using the Poynting vector as:

$$\begin{aligned} \boldsymbol{P}_{\mathrm{ce}}^{\mathrm{e}} &= \frac{1}{t} \cdot \mathrm{Re}\left[\left(\underline{\boldsymbol{E}}_z \times \underline{\boldsymbol{H}}_y^*\right)\big|_{x=t/2} - \left(\underline{\boldsymbol{E}}_z \times \underline{\boldsymbol{H}}_y^*\right)\big|_{x=-t/2}\right] \\ &= \frac{\pi f t \left|\boldsymbol{B}_y^{\mathrm{av}}\right|^2}{u} \frac{\sinh(t/\Delta) - \sin(t/\Delta)}{\Delta \cdot (\cosh(t/\Delta) - \cos(t/\Delta))} \end{aligned} \tag{28}$$

where $\underline{\boldsymbol{E}}_z$ is the electrical field intensity vector and $\underline{\boldsymbol{H}}_y$ is the magnetic field intensity vector in the ESS. They can be both calculated with $\boldsymbol{B}_y$ using the Maxwell equations.

When the reaction field is neglected, the eddy current loss density in the ESS can be expressed as:

$$P_{\mathrm{ce}}^n = \sigma t^2 \pi^2 f^2 \left|\boldsymbol{B}_y^{\mathrm{av}}\right|^2 / 6 = k_{\mathrm{e}} f^2 \left|\boldsymbol{B}_y^{\mathrm{av}}\right|^2 \tag{29}$$

Hence, the conductivity of the ESS can be directly calculated with the iron eddy current coefficient obtained at low frequency, which is shown as:

$$\sigma = 6k_{\mathrm{e}} / \left(t^2 \pi^2\right) \tag{30}$$

It should be mentioned that when the excess loss is incorporated into k_{e} using the simple iron loss model having only two terms, σ calculated with (30) maybe not equal to the physical conductivity

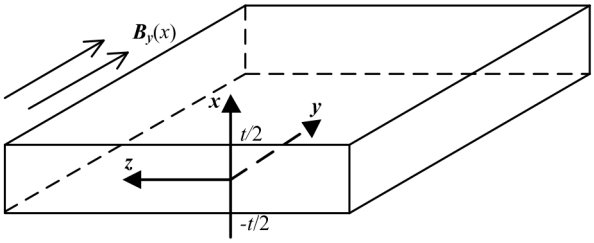

Fig. 23 *Sketch of one ESS*

of the ESS. Equation (30) can only be considered as an engineering estimation of the physical conductivity when it is not easy to measure.

Further, the relationship between the eddy current losses considering and neglecting the eddy reaction effect can be expressed as [9]:

$$P_{\mathrm{ce}}^{\mathrm{e}} = k_{\mathrm{fe}}(f,u)\cdot P_{\mathrm{ce}}^{n} = k_{\mathrm{e}}\cdot k_{\mathrm{fe}}(f,u)\cdot f^{2}\left|\boldsymbol{B}_{\boldsymbol{y}}^{\mathrm{av}}\right|^{2} \tag{31}$$

$$k_{\mathrm{fe}}(f,u) = \frac{3\Delta}{t}\cdot\frac{\sinh(t/\Delta)-\sin(t/\Delta)}{\cosh(t/\Delta)-\cos(t/\Delta)} \tag{32}$$

When considering the uneven distribution of the flux density in the ESS, the hysteresis loss can be calculated with:

$$P_{\mathrm{h}}^{\mathrm{e}} = k_{\mathrm{h}}\cdot f\cdot\frac{1}{t}\int_{-t/2}^{t/2}\boldsymbol{B}_{\boldsymbol{y}}\cdot\boldsymbol{B}_{\mathrm{y}}^{*}\cdot\mathrm{d}x = k_{\mathrm{h}}\cdot k_{\mathrm{fh}}(f,u)\cdot f\left|\boldsymbol{B}_{\boldsymbol{y}}^{\mathrm{av}}\right|^{2} \tag{33}$$

$$k_{\mathrm{fh}}(f,u) = \frac{t}{2\Delta}\cdot\frac{\sinh(t/\Delta)+\sin(t/\Delta)}{\cosh(t/\Delta)-\cos(t/\Delta)} \tag{34}$$